AIAA 2001–0432
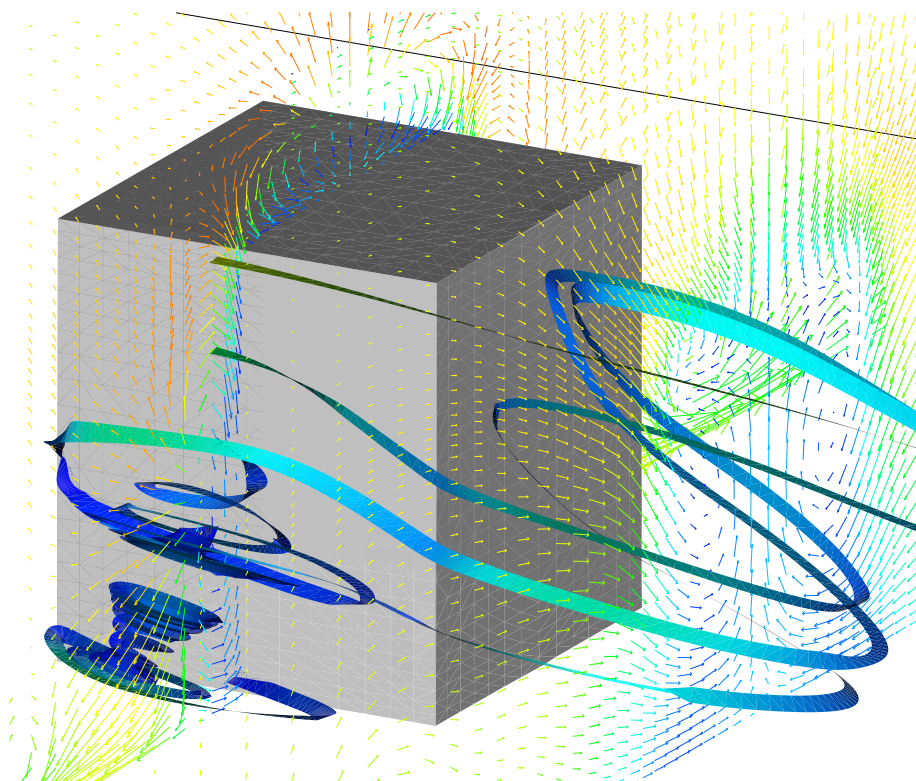
Large Eddy Simulation of the Flow Around a Three-Dimensional Bluff Body

Siniša Krajnović and Lars Davidson
Department of Thermo and Fluid Dynamics, Chalmers University of Technology, SE-412 96 Göteborg, Sweden

39th AIAA Aerospace Sciences Meeting and Exhibit
January 8–11, 2001/Reno, NV

Large Eddy Simulation of the Flow Around a Three-Dimensional Bluff Body

Siniša Krajnović and Lars Davidson
Department of Thermo and Fluid Dynamics, Chalmers
University of Technology, SE-412 96 Göteborg, Sweden

Large Eddy Simulations of the flow around a surface-mounted cube were made. It was shown that it is possible to obtain accurate results at a computational cost of only 60 CPU hours on a SGI R10000. Two one-equation subgrid models are used for modeling the SGS stress tensor. A series of time-averaged velocities and turbulent stresses are computed and compared with the experiments,[1] showing good agreement. Global quantities such as drag and lift coefficients are presented. The transfer of the turbulent energy was studied, and the reverse transfer of energy ("backscatter") was predicted. Coherent structures and other flow features were studied. The results show good agreement with experimental observations.

Introduction

The flow around a three-dimensional bluff body is of great interest in engineering practice. Typical examples of engineering applications are the computation of wind loads on buildings or a simulation of the flow around vehicles. This work is connected to the latter and studies some aspects related to vehicle aerodynamics, such as drag and lift. Most studies of this kind of flow are experimental. Early studies are by Castro and Robins[2] and Hunt *et al.*,[3] and the most recent papers are by Schofield and Logan ,[4] Martinuzzi and Tropea[1] and Hussein and Martinuzzi.[5] Numerical studies are more rare owing to high Reynolds number and poor prediction of this flow using Reynolds-Averaged Navier Stokes (RANS) modeling.

This kind of flow was recently computed using Large Eddy Simulation (LES), and results were presented at two workshops.[6,7] Many of these simulations were performed using extremely fine resolution (more than 10^6 nodes). Near the wall, these simulations approach Direct Numerical Simulation (DNS), resolving the near-wall streaks, and may be described as Quasi-Direct Numerical Simulation (QDNS).[8] Instantaneous results of Large Eddy Simulation of channel flow were used as the inlet boundary condition. This inlet boundary condition provides correct turbulence intensity and shear in the upstream flow. Such a boundary condition can be created for this test case because the Reynolds number is moderate, making LES of the channel flow feasible. In flow with higher Reynolds number (e.g. the flow around bus-like body[9]), it is too costly to obtain this kind of inlet boundary condition.

The purpose of this paper is to present LES of the flow around a surface-mounted cube where the subgrid-scale (SGS) model plays an important role and a relatively coarse mesh is used.

Computational details

The bluff body used in this work is a sharp-edged, surface-mounted cube. The geometry of the computational domain is given in Fig. 1. Interaction of such a body with mean stream flow results in three-dimensional flow even in the mean (see Fig. 2). This can be compared with the flow around two-dimensional bodies (e.g. long cylinder), which is only two-dimensional in the mean.

The Reynolds number was $Re = U_b H/\nu = 40000$ based on the incoming mean bulk velocity, U_b, and the obstacle height, H. The cube is located between $x/H = 0$ and $x/H = 1$ and the channel height is $h = 2H$ (see Fig. 1). A computational domain with an upstream length of $x_1/H = 3$ and a downstream length of $x_2/H = 6$ was used, while the span-wise width was set to $b/H = 7$. The mesh was $82 \times 50 \times 66$ nodes. Near the walls of the channel, $y^+_{min} = 3.7$, while $y^+_{min} = 5.2$ on the top of the cube. The time step was set to 0.02, which gave a maximum CFL number of approximately 2.

Boundary Conditions

The experimental profile (constant in time) was used at the inlet. The lateral boundaries were treated as slip surfaces. At the downstream boundary, the convective boundary condition $\frac{\partial u_i}{\partial t} + c\frac{\partial u_i}{\partial x} = 0$ was used. Here, c is the mean bulk velocity, U_b. No-slip conditions were used at the upper and lower surfaces.
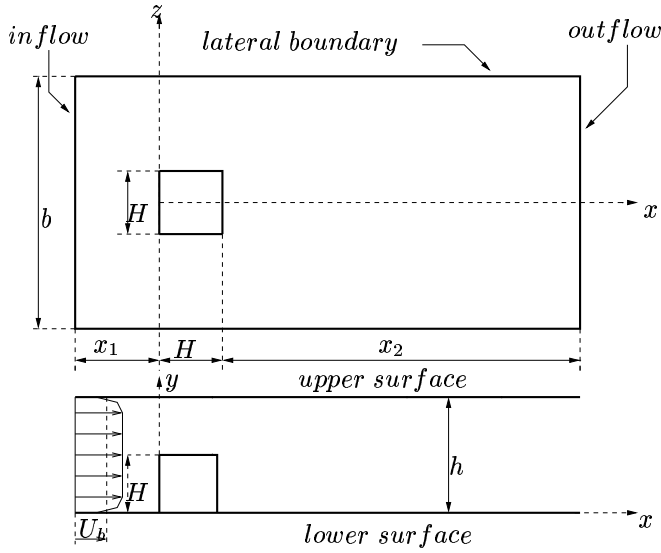
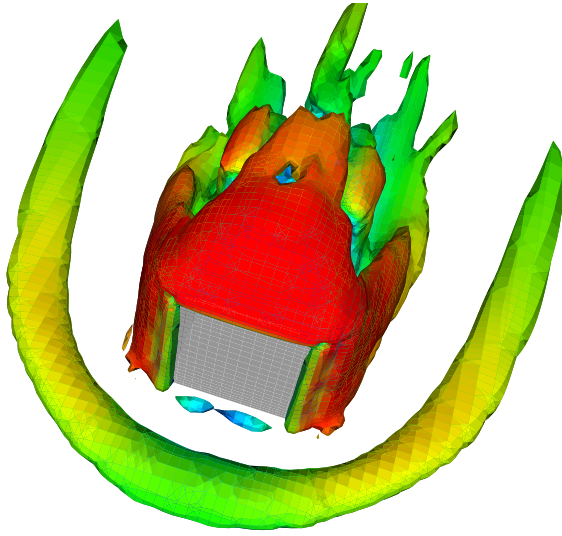**Fig. 1   Geometry of the computational domain.**

Fig. 2   Time-averaged second invariant of the velocity gradient $Q = 0.18$.

Numerical method

This work uses a 3-D finite-volume method for solving the incompressible Navier-Stokes equations. Both convective and viscous plus subgrid fluxes are approximated by central differences of second-order accuracy. A Crank-Nicolson second-order scheme was used for time integration. The momentum equations are solved with the Gauss-Seidel method while a multigrid V-cycle is used for the acceleration of convergence when solving the pressure equation .[10,11]

Subgrid models

Two one-equation subgrid models are used in the present study. Both models are subgrid-scale (SGS) kinetic energy models. The SGS stress tensor is modeled as $\tau_{ij} = -2\nu_{sgs}\bar{S}_{ij}$ with eddy viscosity de-

fined as $\nu_{sgs} = C\Delta k_{sgs}^{\frac{1}{2}}$ and SGS kinetic energy as $k_{sgs} = 1/2\tau_{ii}$.

The first model was developed by Davidson[12] (OEM). This model has also been successfully applied to fully developed channel flow[13] and vortex shedding flow around square cylinders.[14,15] The modeled transport equation for the subgrid kinetic energy, k_{sgs}, reads

$$\frac{\partial k_{sgs}}{\partial t} + \frac{\partial}{\partial x_j}(\bar{u}_j k_{sgs}) = \Pi_{k_{sgs}}$$

$$+\frac{\partial}{\partial x_j}\left(\left(C_{hom}\Delta k_{sgs}^{\frac{1}{2}} + \nu\right)\frac{\partial k_{sgs}}{\partial x_j}\right) - C_*\frac{k_{sgs}^{\frac{3}{2}}}{\Delta}. \quad (1)$$

Here,

$$C = -\frac{\mathcal{L}_{ij}M_{ij}}{2M_{ij}M_{ij}}; \quad M_{ij} = \widehat{\Delta}K^{\frac{1}{2}}\widehat{\bar{S}}_{ij} - \Delta\widehat{k_{sgs}^{\frac{1}{2}}\bar{S}_{ij}};$$

$$K = \widehat{k_{sgs}} + \frac{1}{2}\mathcal{L}_{ii}; \quad \Pi_{k_{sgs}} = 2C\Delta k_{sgs}^{\frac{1}{2}}\bar{S}_{ij}\bar{S}_{ij} \quad (2)$$

where $\mathcal{L}_{ij}$ denotes the *dynamic* Leonard stresses and $K \equiv 1/2T_{ii}$ is the subgrid kinetic energy on the test level. An overbar denotes a grid filter with filter width Δ whereas $\frown$ is a test filter with filter width $\widehat{\Delta} = 2\Delta$. To ensure numerical stability, a constant value of C in space, C_{hom}, is used in the momentum equations and in the diffusion term in Eq.1. C_{hom} is computed with the requirement that the SGS dissipation of the resolved kinetic energy, $\Pi_{k_{sgs}}$, in the whole computational domain remains the same as with the local coefficient, C, i.e.

$$\langle 2C\Delta k_{sgs}^{\frac{1}{2}}\bar{S}_{ij}\bar{S}_{ij}\rangle_{xyz} = 2C_{hom}\langle\Delta k_{sgs}^{\frac{1}{2}}\bar{S}_{ij}\bar{S}_{ij}\rangle_{xyz} \quad (3)$$

where $\langle\rangle_{xyz}$ denotes space-averaging.

The dissipation coefficient for time step $n+1$ has the form

$$C_*^{n+1} = \left(\Pi_K - \widehat{\Pi}_{k_{sgs}} + \frac{1}{\Delta}\widehat{C_*^n k_{sgs}^{\frac{3}{2}}}\right)\frac{\widehat{\Delta}}{K^{\frac{3}{2}}} \quad (4)$$

with

$$\Pi_K = 2C\widehat{\Delta}K^{\frac{1}{2}}\widehat{\bar{S}}_{ij}\widehat{\bar{S}}_{ij}. \quad (5)$$

All local dynamic information is included through the source terms. This is physically more sound since large local variations in C appear only in the source term, and the effect of the large fluctuations in the dynamic coefficients will be smoothed out. The coefficients in the one-equation model affect the stresses in only an indirect way. In the standard dynamic model, the C coefficient is linearly proportional to the stresses, which makes it numerically unstable.

The second model studied in this paper is the localized dynamic k_{sgs}−equation model (LDKM) proposed by Menon and Kim.[16] In the LDKM, the following transport equation is solved:

$$\frac{\partial k_{sgs}}{\partial t} + \frac{\partial}{\partial x_j}(\bar{u}_j k_{sgs}) = \Pi_{k_{sgs}}$$

$$+\frac{\partial}{\partial x_j}\left(\left(C\Delta k_{sgs}^{\frac{1}{2}} + \nu\right)\frac{\partial k_{sgs}}{\partial x_j}\right) - C_* \frac{k_{sgs}^{\frac{3}{2}}}{\Delta} \quad (6)$$

where

$$C = \frac{1}{2}\frac{\mathcal{L}_{ij}\sigma_{ij}}{\sigma_{ij}\sigma_{ij}}; \; \sigma_{ij} = -\widehat{\Delta}\, k_{test}^{\frac{1}{2}}\widehat{\bar{S}_{ij}}; \; k_{test} = \frac{1}{2}\mathcal{L}_{ii} \quad (7)$$

and

$$C_* = \frac{\widehat{\Delta}}{k_{test}^{\frac{3}{2}}}(\nu + \nu_{sgs})\left(\widehat{\frac{\partial \bar{u}_i}{\partial x_j}\frac{\partial \bar{u}_i}{\partial x_j}} - \frac{\partial \widehat{\bar{u}_i}}{\partial x_j}\frac{\partial \widehat{\bar{u}_i}}{\partial x_j}\right) . \quad (8)$$

One-equation SGS models offer a number of advantages over the standard dynamic model:

1. One-equation models can predict backscattering. In the standard dynamic model the dynamic coefficient must be averaged in some homogeneous direction or be clipped in an *ad hoc* manner. This averaging and clipping implies often $\nu + \nu_{sgs} \geq 0$, i.e. $\Pi_{k_{sgs}} \geq -2\nu\bar{S}_{ij}\bar{S}_{ij}$. Thus the backscattering is restricted.

2. In the Germano model the dynamic coefficient must be clipped and/or averaged in the homogeneous direction(s). The local values of the dynamic coefficients can be used in one-equation models.

3. Although it is necessary to solve an additional transport equation, one-equation models are often computationally cheaper than the Germano model thanks to greater numerical stability.[14,17]

The one-equation models include memory effects. Nevertheless, we use these models essentially for stability reasons.

Results

Statistics of the mean flow

A series of time-averaged resolved velocities and turbulent stresses are computed and compared with the experiments. The results for the velocities are generally in much better agreement with the experiment than the stresses. Some results are presented in Figs. 3 and 4. Results for other positions and for $\langle u'^2\rangle_t$ and $\langle v'^2\rangle_t$ are presented in Ref. 18. As can be seen, the predictions

made without a model give poor agreement, whereas the two subgrid models give good agreement with experiments. The separation region at the top of the cube without a model is much too thin (see Fig. 3). This is probably because, without a model, the resolved fluctuations are not damped by any subgrid viscosity, and the resolved fluctuations consequently become too large. This gives excessively large turbulent diffusion, making the separation region smaller and thinner. It can be seen in Fig. 4 that the resolved shear stress $\langle u'v'\rangle_t$ without a model is not larger than those obtained with a model; however, care should be taken in comparing these since the time-averaged velocity fields are very different. Instead, we could argue as follows: the resolved shear stress without a model is of the same magnitude as with a model, although the velocity gradient of the time-averaged velocity field without a model is much smaller; thus, taking into account the difference in the time velocity fields, the resolved shear stress without a model is indeed larger. Both one-equation models gave similar results.

The effect of the models is noticeable in a comparison with the calculation without a model. These differences are especially visible close to the roof of the cube and far downstream. The case studied in this paper was a test case at the 6th ERCOFTAC/IAHR/COST Workshop[6] using RANS models. The velocity profiles, especially further downstream of the cube, are much better predicted by LES in the present work. The turbulence stresses are in significantly better agreement with the experimental values.

Numerical wiggles are present in the mean velocity profile $\langle \bar{u}\rangle_t$ for $x/H = -1.0$, as can be seen in Fig. 3. This is probably due to a combination of coarse mesh in that part of the domain and use of the central differencing scheme. In the case of shear stresses, both the resolved quantity $\langle u'v'\rangle_t$ and the SGS quantity $\langle \tau_{12}\rangle_t$ were computed as suggested by Reynolds.[19] Similar results for the total (i.e. resolved plus SGS) shear stresses from LES using Smagorinsky model are shown in Krajnović.[20] We also computed $\langle u'^2\rangle_t + \langle \tau_{11}\rangle_t$, $\langle v'^2\rangle_t + \langle \tau_{22}\rangle_t$ and $\langle w'^2\rangle_t + \langle \tau_{33}\rangle_t$ and compared them with the experiments. The total (i.e. resolved plus SGS) turbulent stress are not shown here because we found that the difference between these and resolved mean turbulent stress is almost negligible.

In Fig. 5, the oil-film visualization by Martinuzzi and Tropea[1] is compared with streamlines projected onto the floor. The predicted streamline pictures show most of the details observed in the experiments. In the experiments, Martinuzzi and Tropea observed three main curves in front the cube. Curve A corresponds to the primary, upstream se-
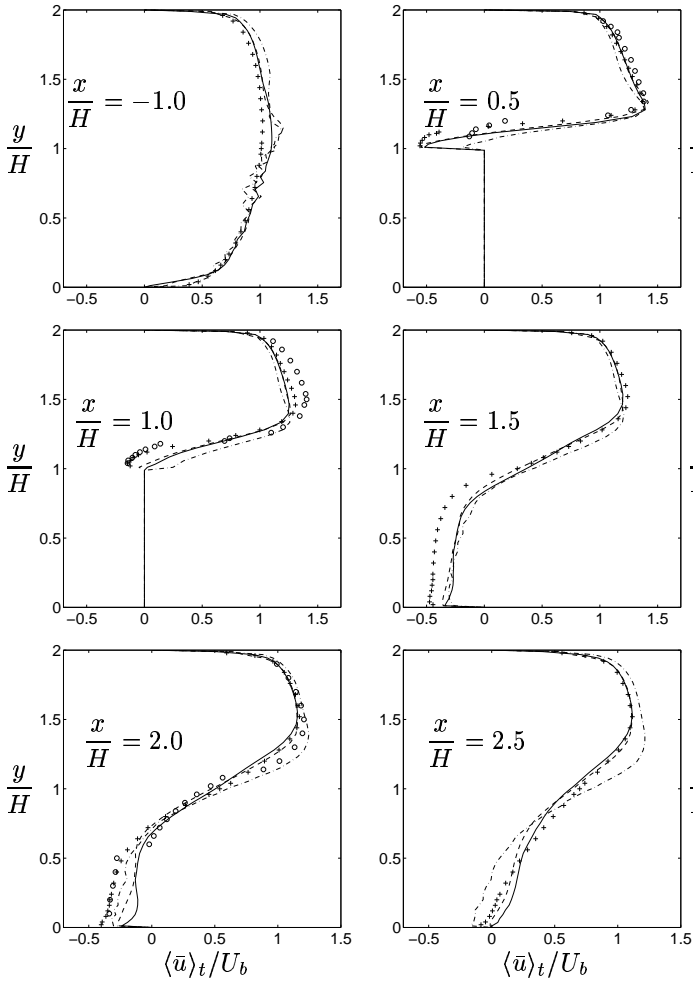
Fig. 3 Comparison between OEM (dashed line), LDKM (solid line) and calculation without model (dashed-dotted line). Experiments[1] (*o* and +).

Fig. 4 Comparison between OEM (dashed line), LDKM (solid line) and calculation without model (dashed-dotted line). Experiments[1] (+).

paration curve and curve B corresponds to the approximate time-averaged location of the horseshoe vortex. Curve C indicates a secondary recirculation at the front base of the cube.[1] Curves A and C are clearly visible in the picture of the predicted streamlines, while curve B is somewhat weaker. The uncertainty of the experiment in this region is very large, and the flow between curves A and B is unstable. From this we conclude that it is not clear whether experiments or LES give better results in this part of the domain. The contour of the recirculation downstream of the cube is also clearly visible.

Because of the inability to average over statistically equivalent points, the symmetry was used as a measure of whether the simulation was run for a sufficiently long time. The averaging time in the simulation was $tH/U_b = 300$ (7500 time steps). As can be seen in Fig. 5, the surface streamlines downstream the cube are symmetric, which indicates that the number of averaging samples is sufficient. Figure 6 plots the streamlines in the
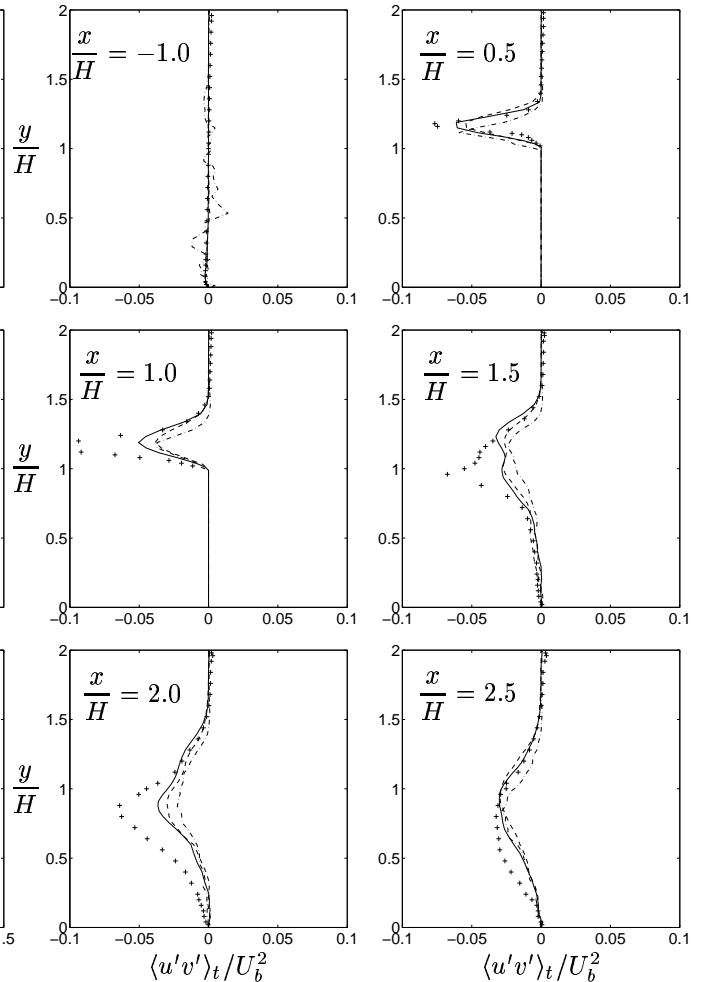
Model	X_{F1}	X_T	X_{R1}
Exp.	1.04	-	1.61
OEM	0.97	0.95	1.44
LDKM	1.06	0.95	1.38

Table 1 Lengths for re-attachment and separation (see Fig. 7a).

symmetry plane. The vortices on the top and behind the cube and the head of the horseshoe are clearly visible in this picture. The re-attachment length, X_{R1}, and separation lengths, X_{F1} and X_T (Fig. 7a), are determined from the distribution of the skin friction coefficient, $C_f = 2\tau_w/\rho U_b$, shown in Fig. 7b. Comparisons of different time-averaged recirculation lengths with experiments are shown in Table 1.

Global Quantities

The mean and RMS drag and lift coefficients are presented in Table 2. The time history of C_D and C_L is given in Fig. 8. There are no experimental values for drag and lift coefficients known to the authors. The values of mean and RMS values for
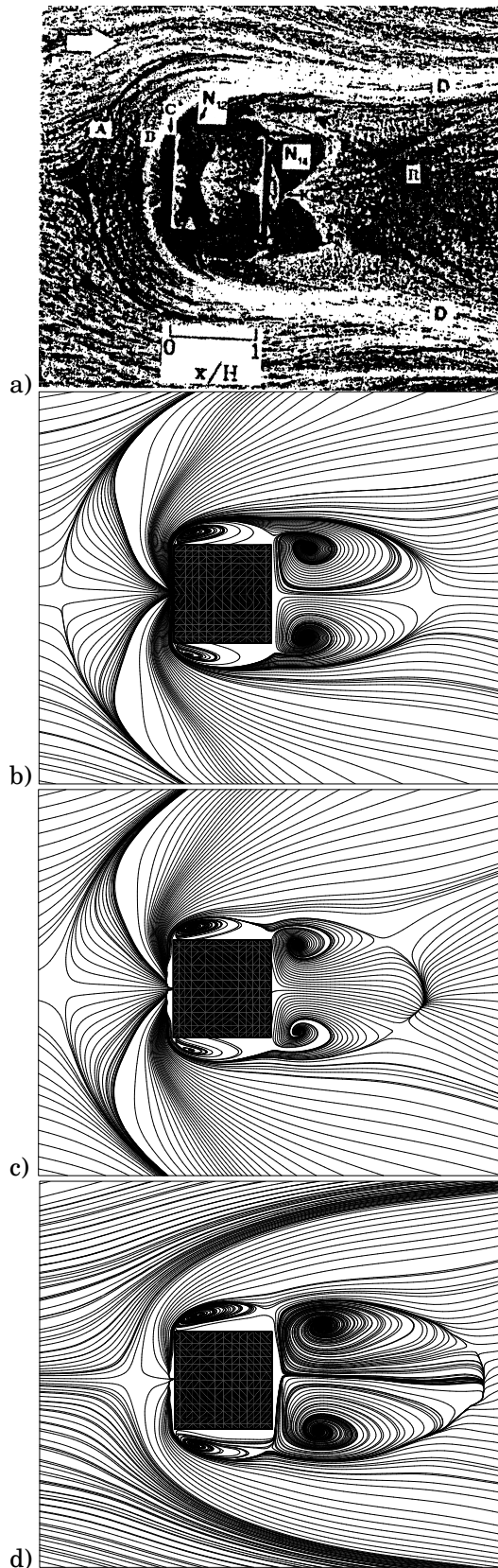
Fig. 5 a) Oil-film visualization by Martinuzzi and Tropea compared with streamlines of the mean flow projected onto the channel floor for LES with b) OEM, c) LDKM and d) without a model.
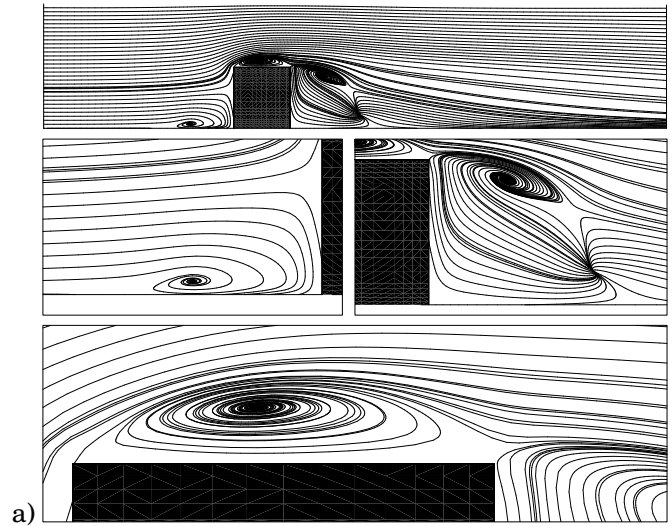
Exp.(u-v)
Mesh A

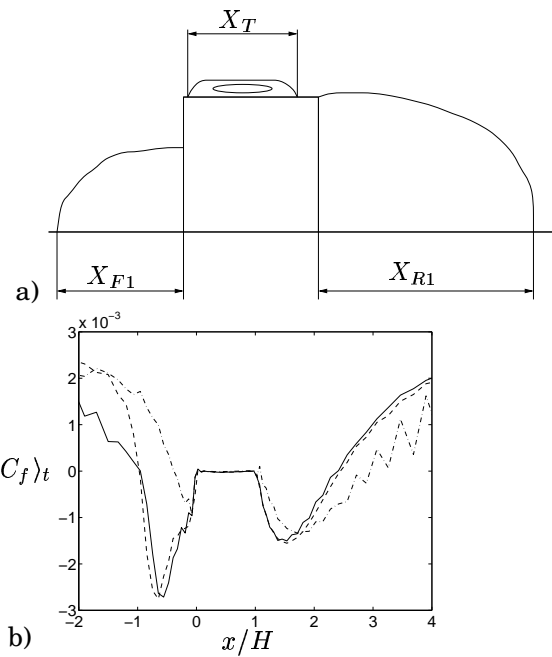Fig. 6 Streamlines of the mean flow projected onto the center-plane of the cube using LDKM.

Fig. 7 a) Re-attachment and separation lengths. b) Time-averaged skin friction coefficient on the channel floor and roof of cube. Solid line: LDKM; dashed line: OEM; dashed-dotted line: no model

Model	$\langle C_D \rangle_t$	$C_{D,rms}$	$\langle C_L \rangle_t$	$C_{L,rms}$
Exp.	-	-	-	-
OEM	1.14	0.062	0.92	0.038
LDKM	1.16	0.070	0.91	0.040

Table 2 Mean and RMS values of drag and lift coefficients.
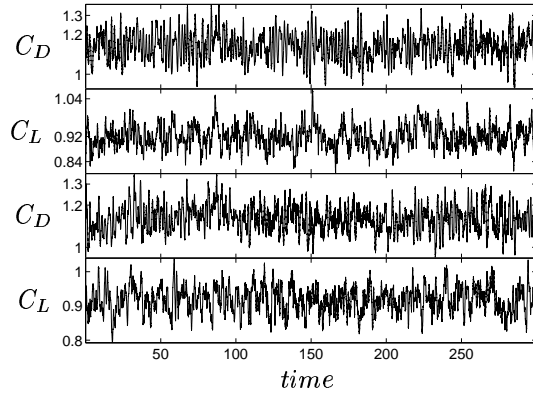
Fig. 8 Time history of C_D and C_L using OEM (above) and LDKM (below).

OEM and LDKM are very similar.

Mesh A

Fig. 9 Isosurface of the instantaneous SGS dissipation of $\bar{k}$, $\Pi_{k_{sgs}} = -1$ in OEM.

SGS dissipation of the resolved kinetic energy

Special care was given to the phenomenon of "backscatter". It is well known that, in addition to the transport of the turbulent energy from large to small scales, the reverse transport is also possible ("backscatter"). In the Smagorinsky model the SGS dissipation of the resolved kinetic energy, $\bar{k}$, is $\Pi_{k_{sgs}} = -\tau_{ij}\bar{S}_{ij} \geq 0$, i.e. the model is purely dissipative. Both one-equation models used in this work are able to predict negative SGS dissipation of $\bar{k}$, indicating "backscatter". Depending on how large a fraction of the total energy transport is contained in the reverse transport, backscatter can be of importance. Constant C in the model for the SGS dissipation of $\bar{k}$ is permitted to be negative in both OEM and LDKM. When C becomes negative, it represents modeled "backscatter". The SGS dissipation of $\bar{k}$, $\Pi_{k_{sgs}}$, was studied instantaneously in Fig. 9 and in a time-averaged way in Figs. 10 and 11. The LDKM gives a smaller magnitude of negative $\Pi_{k_{sgs}}$ than OEM. The strongest backscatter occurs near the front vertical corners, see Figs. 9, 10 and 11. The lower values of negative $\Pi_{k_{sgs}}$ follow the horseshoe in the case of OEM, Fig. 10b. Two isosurfaces of the mean SGS dissipation term for LDKM are shown in Fig. 11. It can be seen in Fig. 11a that the strongest backscatter is more uniformly distributed near the front vertical corners than in OEM.

It can be seen in Fig. 11b that LDKM predicts backscatter far upstream of the cube, in regions where the grid is refined. Thus LDKM seems to be more sensitive to grid refinement than OEM. This is because LDKM is more local than OEM. One can also find low-value backscatter located in the recirculation zone in front and on the roof of the cube, Fig. 11b.

To explain the reasons for negative $\Pi_{k_{sgs}}$, we computed the numerator in the expression of C in Eq. 2, $\langle \mathcal{L}_{ij}M_{ij}\rangle_t$, in the position of the strong-
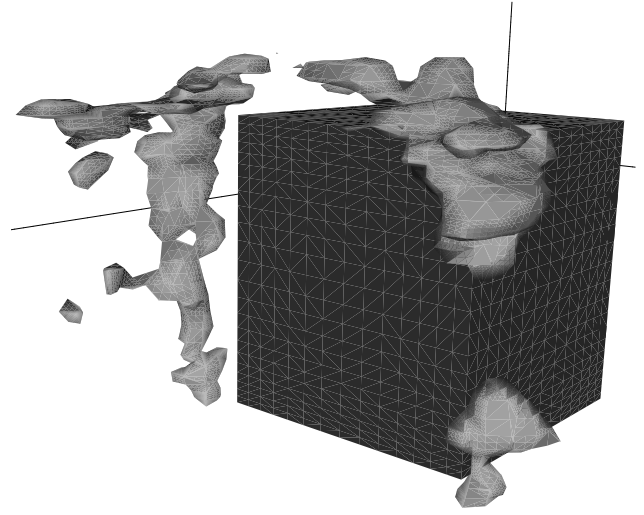
est backscatter. It can be seen in Fig. 12a that, in the regions of strongest negative $\langle\Pi_{k_{sgs}}\rangle_t$, $\langle\mathcal{L}_{12}M_{12}\rangle_t$ and $\langle\mathcal{L}_{13}M_{13}\rangle_t$ are the dominant terms. $\mathcal{L}_{13}$ is the most important negative term, as is shown in Fig. 12b.

Numerical stability

The time history of the dynamic coefficient, C, and the dissipation coefficient, C_*, is shown for the two subgrid models in Fig. 13. It can be seen that the time history of C is much smoother for LDKM than for OEM. In OEM, similarity assumptions are made between the grid level (length scale $\ell < \Delta$, velocity scale $k_{sgs}^{\frac{1}{2}}$) and the test level (length scale $\ell < \widehat{\Delta}$, velocity scale $K^{\frac{1}{2}}$). However, in LDKM, the similarity assumption is made between the grid level and the intermediate level (length scale $\Delta < \ell < \widehat{\Delta}$, velocity scale $[0.5\mathcal{L}_{kk}]^{\frac{1}{2}}$).

The denominator in Eq. 7, $\sigma_{ij}\sigma_{ij}$, does not tend to zero as much as the denominator, $M_{ij}M_{ij}$, in OEM (Eq. 2), which explains why C does not oscillate as much in LDKM. In LDKM, the local coefficient is used in the momentum equation (with the restriction $\nu + \nu_{sgs} \geq 0$), which makes the model less stable. The time history of coefficient C_* in front of the dissipation term (see Eqs. 4 and 8 and Fig. 13) is also smoother in LDKM than in OEM, although the difference is much smaller than for C. The dissipation coefficient often tends toward zero (it is restricted so that $C_* \geq 0$) but never becomes larger than 5.

Sensitivity to grid refinement

Sensitivity to grid refinement in both time and space was studied. A similar study using the Smagorinsky model is reported in Ref. 20. It is very difficult to study sensitivity to grid refinement
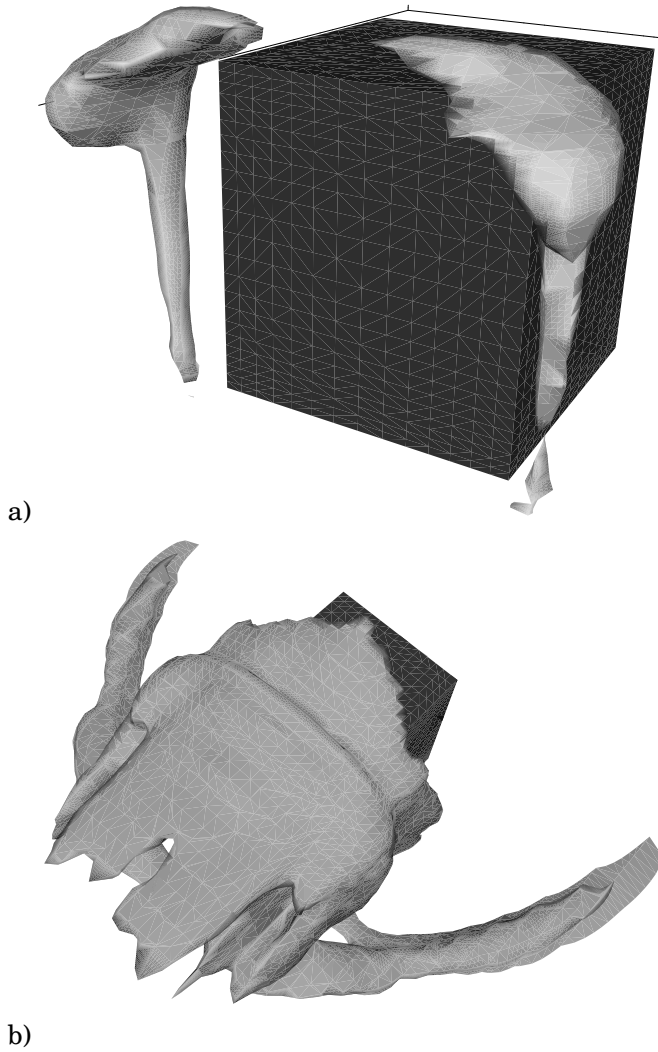
a)

b)

Fig. 10   Isosurface of the time-averaged SGS dissipation of $\bar{k}$ in OEM. a) $\langle \Pi_{k_{sgs}} \rangle_t = -1$, **b)** $\langle \Pi_{k_{sgs}} \rangle_t = -0.05$.

a)

b)

Fig. 11   Isosurface of the time-averaged SGS dissipation of $\bar{k}$ in LDKM. a) $\langle \Pi_{k_{sgs}} \rangle_t = -0.05$, **b)** $\langle \Pi_{k_{sgs}} \rangle_t = -0.01$.

because refining the grid also changes the model. This is because Δ in $\nu_{sgs} = C\Delta k_{sgs}^{\frac{1}{2}}$ is defined as $\Delta = (\Delta_1 \Delta_2 \Delta_3)^{1/3}$. It is possible to define Δ so that it is mesh independent, but this would drastically increase the cost of the calculation. We found that this mesh with only 270600 nodes gave results comparable with results from the workshops,[6,7] where some participants used more than 10^6 nodes.

Physics of The Flow

In experiments, one is often limited to measuring flow quantities in only one point or plane. From large eddy simulation, we obtain the instantaneous flow-field in the whole computational domain. This makes it possible to make a very detailed study of the flow. In this section, we study the physics of the flow and compare our findings with the results of the experiments.[1,5]

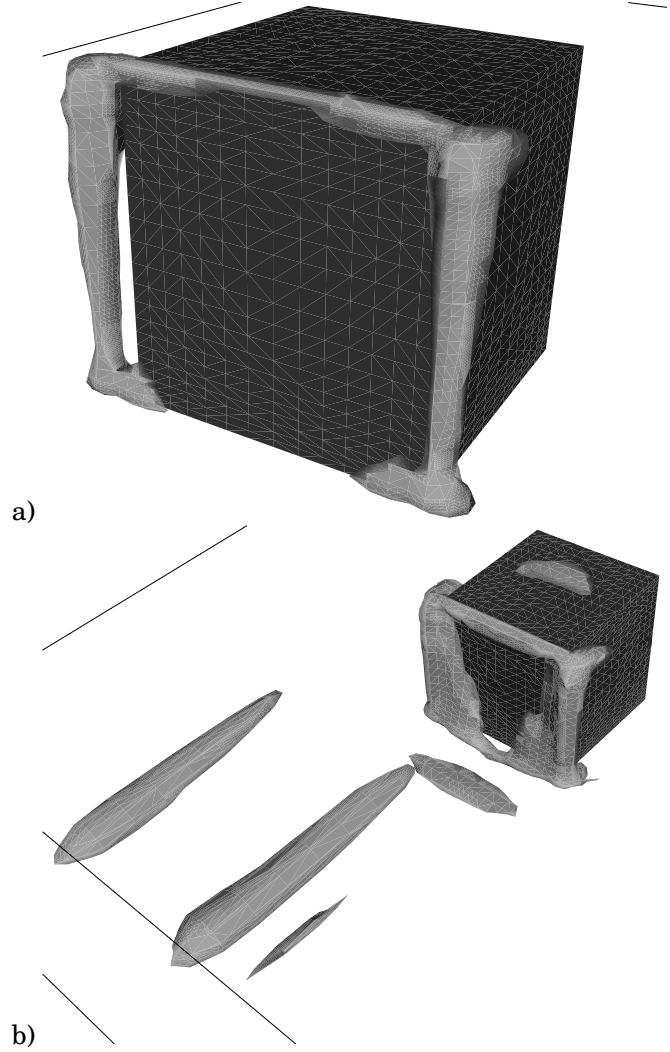We found that the flow around a surface-mounted cube is complex and re-attachment occurs both on

the top of the cube, lateral surfaces and behind the cube in Figs. 5 and 6. This flow complexity is caused by vortices generated in the shear layer on the top and the lateral sides of the cube (see Fig. 14).

The main features of this flow are:

1. the horseshoe vortex

2. the secondary corner vortex upstream of the cube

3. lateral vortices

4. the vortex system on the top of the cube

5. the secondary vortex behind the cube

6. two recirculation vortices behind the cube

The horseshoe vortex

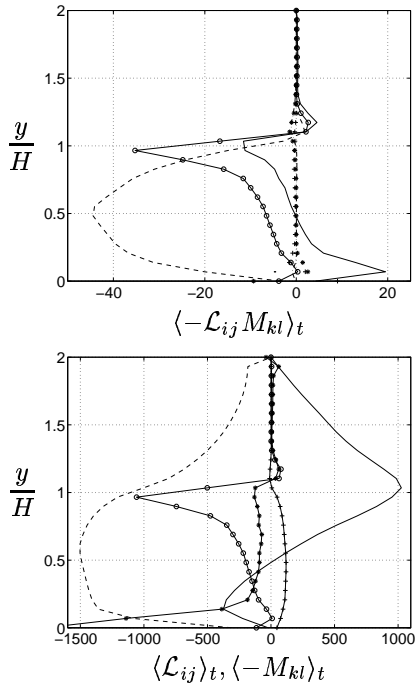The horseshoe vortex on the lower channel wall is shown in the mean in Fig. 2 and instantaneous in

AMERICAN INSTITUTE OF AERONAUTICS AND ASTRONAUTICS PAPER 2001–0432

Fig. 12 $x/H = -0.2$, $z/H = 0.6$. **OEM. a)** $\langle \Pi_{k_{sgs}} \rangle_t / 300$ is denoted by $-o$. $\langle -\mathcal{L}_{12} M_{12} \rangle_t$ **(solid line),** $\langle -\mathcal{L}_{13} M_{13} \rangle_t$ **(dashed line),** $\langle -\mathcal{L}_{22} M_{22} \rangle_t$ **(dashed-dotted line),** $\langle -\mathcal{L}_{23} M_{23} \rangle_t$ **(∗∗),** $\langle -\mathcal{L}_{33} M_{33} \rangle_t$ **(++); b)** $\langle \Pi_{k_{sgs}} \rangle_t / 10$ **is denoted by** $-o$. $\langle \mathcal{L}_{12} \rangle_t$ **(solid line),** $\langle \mathcal{L}_{13} \rangle_t$ **(dashed line),** $\langle -M_{12} \rangle_t / 3$ **(−∗),** $\langle -M_{13} \rangle_t$ **(−+).**

Mesh A
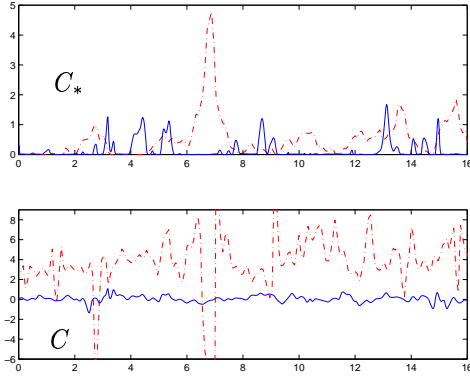
Fig. 13 Time history of dynamic coefficients C_* **and** C**. Solid line: LDKM; dashed-dotted line: OEM.**

Fig. 15. In these figures, the horseshoe vortex and other coherent structures are visualized with the second invariant of the velocity gradient Q. The second invariant of the velocity gradient Q is defined as

$$Q = -\frac{1}{2} \frac{\partial \bar{u}_i}{\partial x_j} \frac{\partial \bar{u}_j}{\partial x_i} = -\frac{1}{2} \left(\bar{S}_{ij} \bar{S}_{ij} - \bar{\Omega}_{ij} \bar{\Omega}_{ij} \right) \qquad (9)$$

where $\bar{\Omega}_{ij}$ is the anti-symmetric part of the resolved velocity gradient tensor.[21]

The position of the horseshoe vortex on the lateral side of the cube can be seen in Fig. 16a. This was compared with the results of Hussein and Martinuzzi[5] shown in Fig. 16b. We found that the position of the horseshoe leg in the plane $x/H = 1.75$
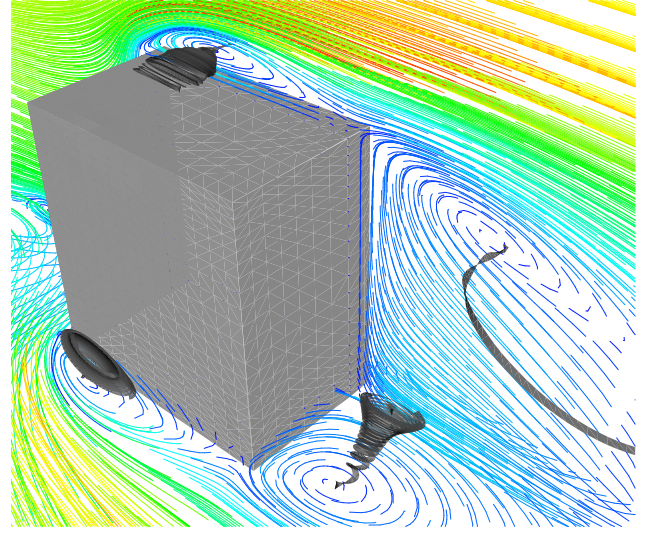

Fig. 14 Vortices generated in the shear layer. Time-averaged velocity planes $y/H = 0.02$ **and** $z/H = 0$**. The face to the right is the downstream face of the cube.**

is $z/H \approx 1.7$ while in the experiment the position of the horseshoe leg is $z/H \approx 1.25$. To explain this difference in the location of the horseshoe legs we refer to findings by Castro and Robins.[2] They found that the shape of the horseshoe vortex is influenced by the oncoming boundary layer. As already mentioned, we used the experimental velocity profile (constant in time) as the inlet boundary condition. Probably, only a real, fully developed channel flow inlet boundary condition can give the correct boundary layer thickness. The difference in the position of the horseshoe vortex between the experiments and the LES simulation is probably caused by the incorrect inlet boundary condition. We have also observed that LES simulation without a model gives a smaller distance between the two legs of the horseshoe vortex than does simulation with one-equation models, see Fig. 5.

The secondary corner vortex upstream of the cube

The secondary corner vortex upstream of the cube can be seen in Fig. 2. The position of this corner vortex is discussed in section "Statistics of the mean flow" as curve C.

Lateral vortices

We observed two recirculation regions formed by the lateral vortices in Fig. 5. These are here shown as streamlines of the mean flow projected onto the channel floor. There centers are located at $x/H \approx 0.2$, $z/H \approx \pm 0.6$. One of these recirculation regions is shown in Fig. 17 as a time-averaged velocity vectors in plane $z/H = -0.55$. These recirculation regions are approximately of the same size, shape and position in our LES with OEM and LDKM (Figs. 5b and 5c). In LES without a mo-
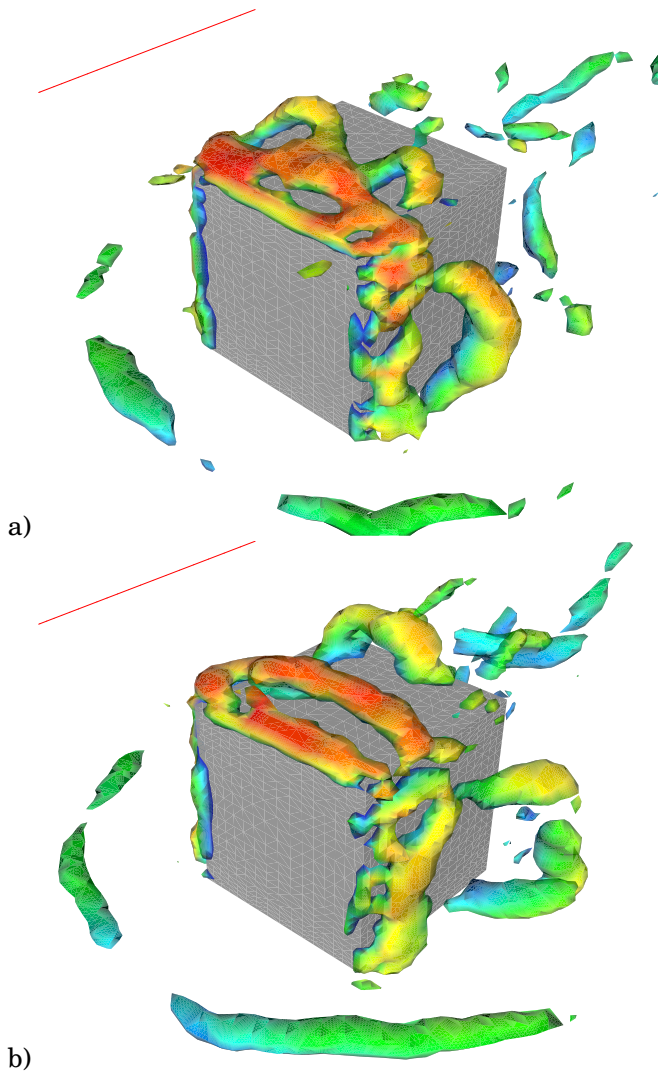
Fig. 15   Instantaneous second invariant of the velocity gradient $Q = 5$ colored with the velocity magnitude with two different times.

del in Fig. 5d, these recirculation regions are longer and tilted compared with the ones in simulations with OEM and LDKM.

We visualized the lateral vortices using the second invariant of the velocity gradient Q and followed their lifespan from the formation close to the front vertical edge of the cube to the breakdown close to the rear vertical edge of the cube. We made a number of movies for this study (see Ref. 18). Here, we are limited to showing only some snapshots in Fig. 15, with a fully developed lateral vortex in Fig. 15a and breakdown of this vortex in Fig. 15b. The lateral vortex is nicely shown in Fig. 15a, and it has the shape of the ear of a tea cup. At approximately 80% of the cube height (the tea cup), the vortex (the ear) attaches to the lateral side of the cube, which can also be seen in Fig. 17. The lateral vortex (Fig. 15) attaches to the lower channel wall close to the cube, which can also be
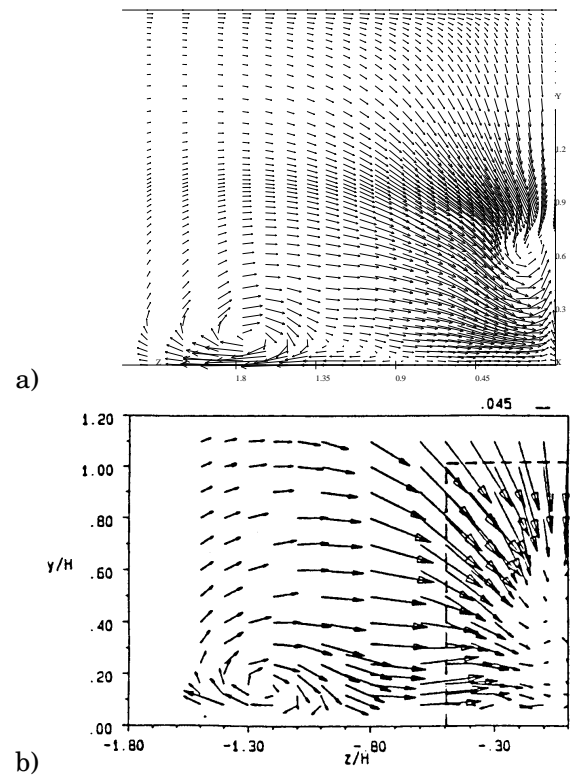
Fig. 16   Time-averaged velocity field in the plane $x/H = 1.75$ in: a) LES using OEM; b) experiment.
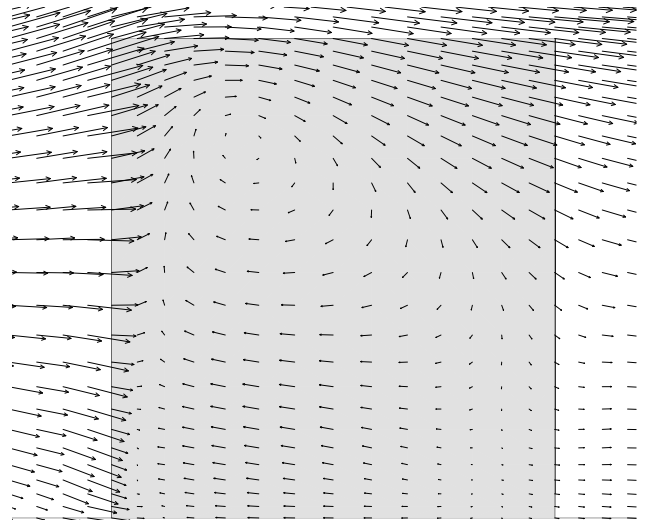

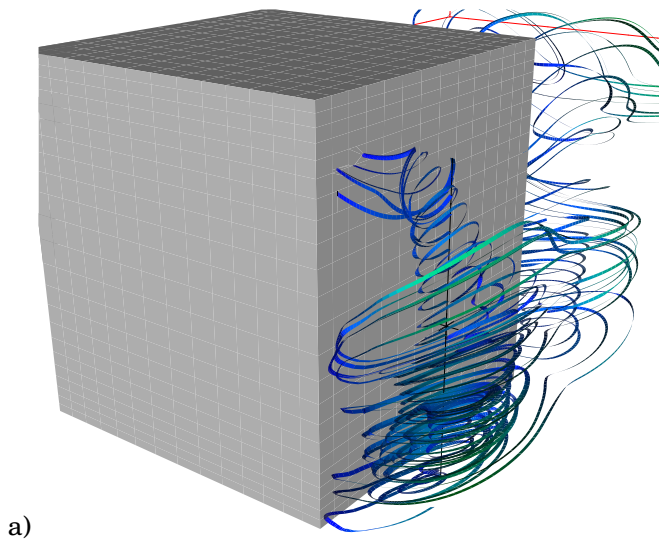Fig. 17   Time-averaged velocity vectors in plane $z/H = -0.55$.

AMERICAN INSTITUTE OF AERONAUTICS AND ASTRONAUTICS PAPER 2001–0432

a)

Fig. 18 Time-averaged streamlines showing the lateral vortex.

Fig. 19 Time-averaged streamlines on the top of the cube.

seen in Fig. 14.

In the mean, as mentioned before, this vortex forms a vortex near junction of the channel floor and the cube shown in Fig. 18. The position of this vortex is here visualized using streamlines, which show a vortex stretching from the lateral wall to the floor. The attachment of this vortex on the lateral side of the cube can be compared with the focus in Fig. 17.

The vortex system on the top of the cube

There is a multiple vortex system on the top of the cube, shown instantaneously in Fig. 15 and in the mean in Figs. 19 and 20. Again in Fig. 15, we can see how these vortices are formed at and shed from the upper front edge and how their shape changes during the time. These vortices form in the mean two cone-like structures with their base close to the position $z/H = 0, y/H = 1.1$ and their nibs attached on the top of the cube near the lateral sides. These structures are visualized in Fig. 19 using streamlines. The same structures are indicated in Fig. 20 using mean velocity vectors in plane $y/H = 1.02$. Again the attachment of the cone-like vortices on the top of the cube in Fig. 19 is correlated with the position of the recirculation foci (the nibs) in Fig. 20. Martinuzzi and Tropea[1] found that these vortices result in complicated surface shear stress patterns. These shear stress patterns were studied here in the mean in Fig. 21. As expected, surface shear stress, τ_w, is correlated with the mean velocity in the boundary layer (see Figs. 20 and 21). We found that the largest values of τ_w in the mean are in the separation region on the top of the cube and at the corners of the cube (see Fig. 21). The latter is a result of the large velocity gradients at the corners of the cube.
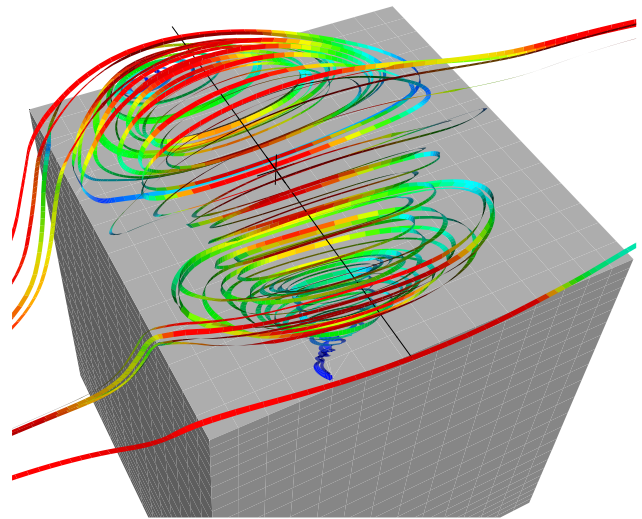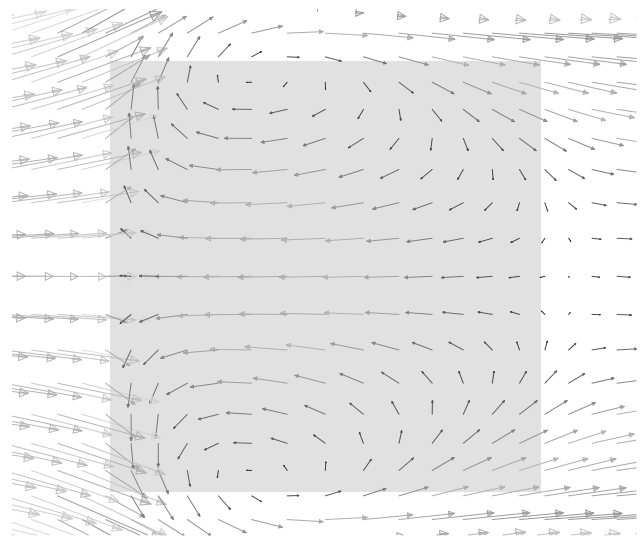

Fig. 20 Mean velocity vectors in plane $y/H = 1.02$.

The secondary vortex behind the cube

The secondary vortex behind the cube is shown in Fig. 22. This vortex is visualized here using mean velocity vectors and vorticity isolines in the plane $z/H = 0$.

Recirculation vortices behind the cube

The wake flow was studied thoroughly both instantaneously and in the mean. Both stream-wise vortices behind the cube are shown in Figs. 23, 24 and 25. Studying Figs. 23 and 24 we find that the axes of the back vortices are tilted with respect to the vertical axes. In Figs. 25 and 26, the suggestion of Martinuzzi and Tropea[1] that these vortices join at the symmetry plane is confirmed.
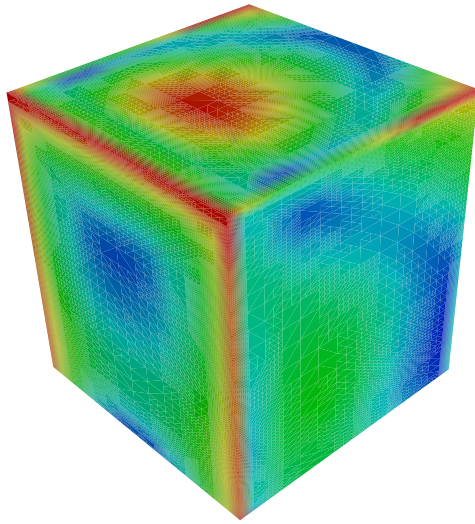
Fig. 21 Mean surface stress. The face to the right is the lateral face of the cube.

Fig. 23 Time-averaged streamlines behind the cube. Time-averaged velocity plane $z/H = 0$. View of downstream face of the cube.
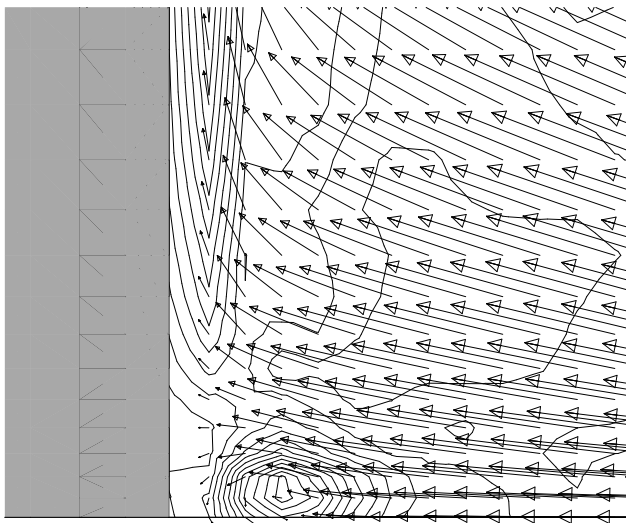

Fig. 22 Time-averaged velocity vectors and vorticity isolines in the plane $z/H = 0$, showing the secondary vortex behind the cube.

The surface pressure

Castro and Robins[2] pointed out that the surface pressure field in the wake region is of great importance for a proper understanding of the flow around surface-mounted bodies. Surface mean pressure is shown in Fig. 27. We found that the surface pressure field, both in the wake and on the top and lateral sides of the body, is highly oscillating (see Fig. 28). The observation by Castro and Robins[2] of the strong pressure gradient close to the leading edges is confirmed in Fig. 29.

Exchange of the fluid between the separation regions

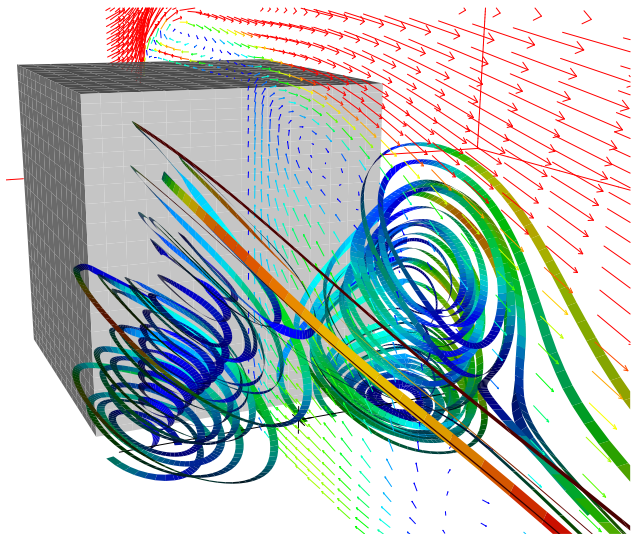Hunt *et al.*[3] observed the exchange of fluid between the separation regions. They concluded
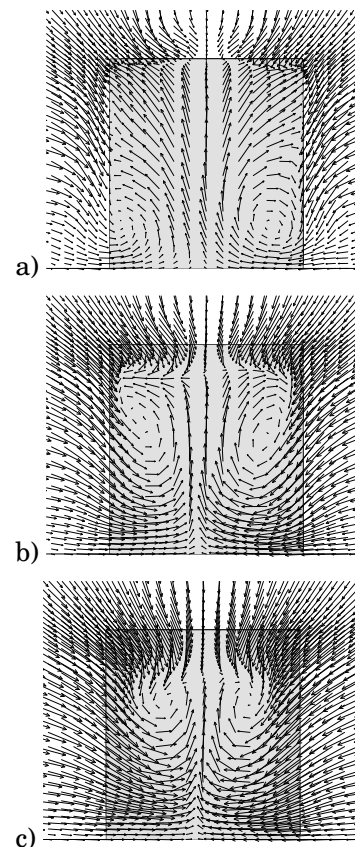

Fig. 24 Time-averaged velocity field in plane: a) $x/H = 1.3$, b) $x/H = 1.5$ and c) $x/H = 1.7$.

a)

b)
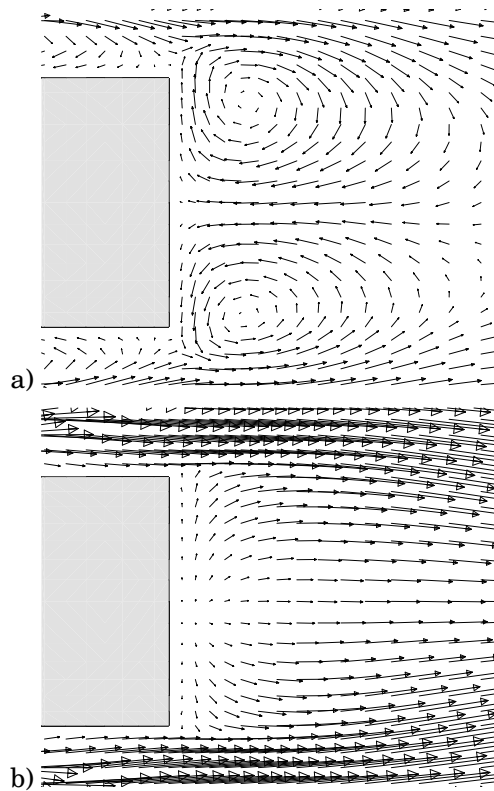
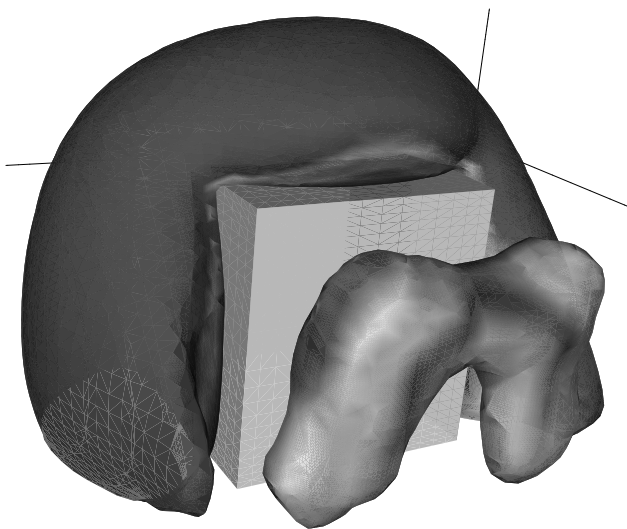**Fig. 25 Time-averaged velocity field in planes a)** $y/H = 0.05$ **and b)** $y/H = 0.95$**.**

Fig. 27   Mean surface pressure. The face to the right is the lateral face of the cube.

Fig. 26   Time-averaged pressure isosurface $p = -0.22$**. View of downstream face of the cube.**
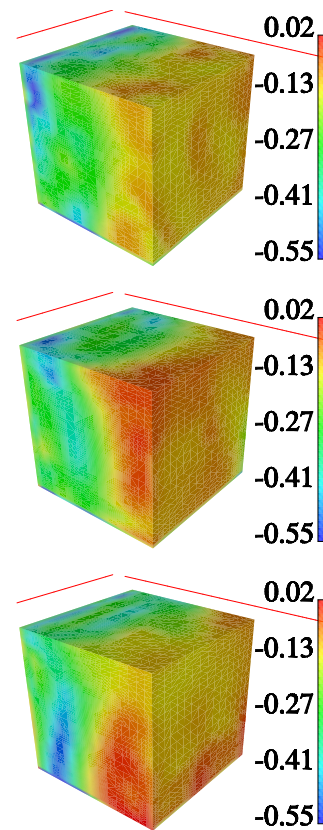

Fig. 28   Surface pressure with three different times. The face to the right is the downstream face of the cube.
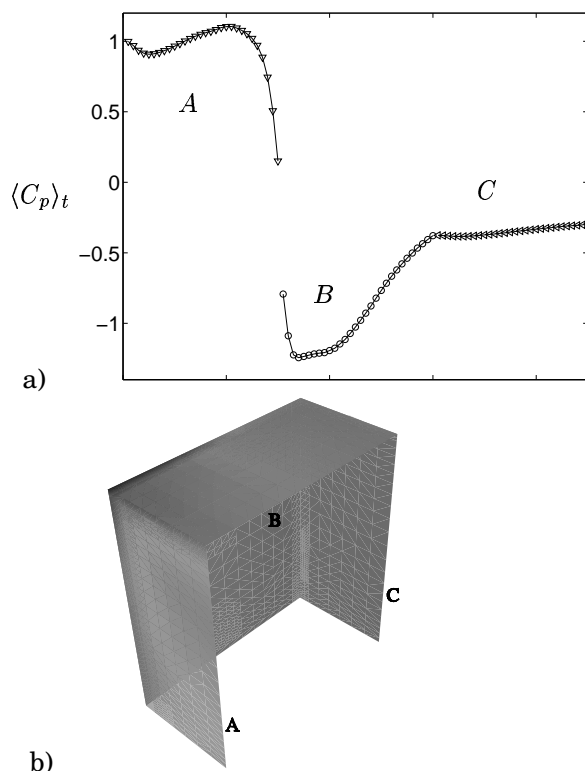
a)

b)

Fig. 29   Point "A" is located at x/H=0. OEM. a) Time-averaged surface pressure coefficient $\langle C_p \rangle_t$ computed along the line ABC shown in b).

Fig. 30   Exchange of the fluid between lateral and back vortices. View of lateral face and downstream face of the cube.

Fig. 31   Simulated hydrogen bubbles.

that the separation region in the flow around a three-dimensional bluff body cannot be closed. To come to this conclusion, they used a surface oil-film visualization. Their results are confirmed in Fig. 30. Here, we have plotted two velocity vector planes at $x/H = 0.5$ and $x/H = 1.5$. We can see how the streamlines stretch from the lateral vortices to the back vortices, showing the exchange of the fluid between vortices. This phenomenon was also studied instantaneously using simulated hydrogen bubbles (see Ref. 18).

Mimicking the experiments

Using LES results one can make visualization similar to the visualizations obtained in more traditional experimental techniques. We simulated particle traces in Fig. 31. This can be compared with the experiments with hydrogen bubbles. We found that some "bubbles" lose their kinetic energy and attach on the front face of the cube in Fig. 31. Some "bubbles" are convected downstream in spiral motion forming the horseshoe vortex (see Fig. 31). Other "bubbles" in the shear layer of the recirculating region behind the cube are attracted by the separation region and can be attached to the rear surface of the cube.
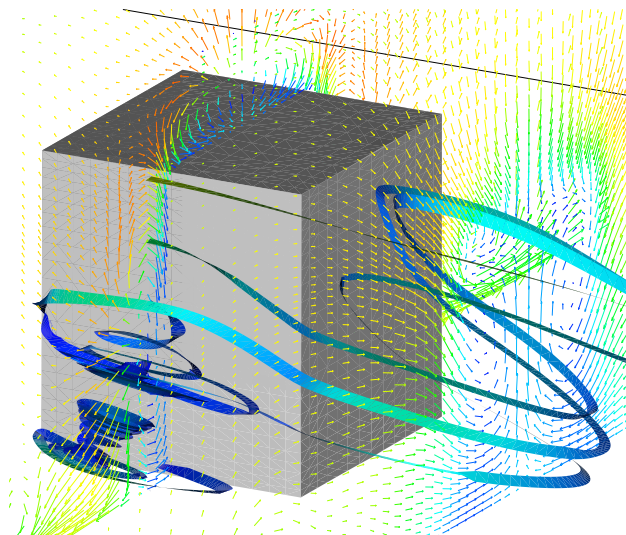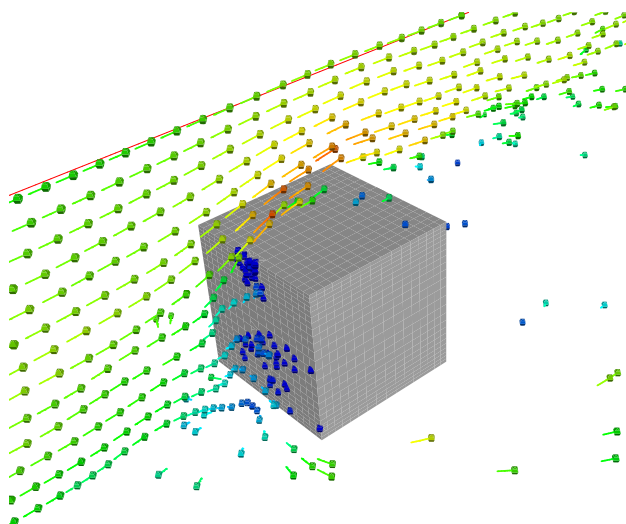
Conclusions

Large Eddy Simulation was used for the simulation of the flow around a three-dimensional bluff body. This flow was studied thoroughly, both in the mean and instantaneously. The inlet boundary condition was the experimental velocity profile constant in time. This leads unavoidably to an incorrect boundary layer thickness upstream of the body. Still, the sharp edges of the obstacle define the separations and minimize the influence of the inlet boundary condition on the statistics.

It was shown that it is possible to obtain accurate results at an acceptable computational cost. The computational cost for the case of the surface-mounted cube is represented by ~ 60 CPU hours on a SGI R10000. Two one-equation subgrid models were compared. Computations with a model gave

better results than computation without a model. The transfer of the turbulent energy was studied, and the reverse transfer of energy ("backscatter") was predicted. Flow features observed in the visualization by Martinuzzi and Tropea[1] are confirmed in this work.

Acknowledgments

References

[1] Martinuzzi, R. and Tropea, C., "The Flow Around Surface-Mounted Prismatic Obstacles Placed in a Fully Developed Channel Flow," *ASME: Journal of Fluids Engineering*, Vol. 115, 1993, pp. 85–91.

[2] Castro, I. P. and Robins, A. G., "The flow around a surface-mounted cube in uniform and turbulent stream," *Journal of Fluid Mechanics*, Vol. 79, 1977, pp. 307–335.

[3] Hunt, J. C. R., Abell, C. J., Peterka, J. A., and Woo, H., "Kinematical studies of the flows around free or surface-mounted obstacles; applying topology to flow visualization," *Journal of Fluid Mechanics*, Vol. 86, 1978, pp. 179–200.

[4] Schofield, W. H. and Logan, E., "Turbulent Shear Flow Over Surface Mounted Obstacles," *ASME: Journal of Fluids Engineering*, Vol. 112, 1990, pp. 376–385.

[5] Hussein, H. and Martinuzzi, R. J., "Energy Balance for Turbulent Flow Around a Surface Mounted Cube Placed in a Channel," *Physics of Fluids A*, Vol. 8, 1996, pp. 764–780.

[6] Hanjalić, K. and Obi, S., "ERCOFTAC/IAHR/COST Workshop on Refined Flow Modeling," Delft University of Technology, 1997.

[7] Rodi, W., Ferziger, J. H., Breuer, M., and Pourquié, M., "Workshop on LES of Flows past Bluff Bodies," Rotach-Egern, Germany, 1995.

[8] Spalart, P. R., "Strategies for turbulence modelling and simulations," *Int. J. Heat and Fluid Flow*, Vol. 21, 2000, pp. 252–263.

[9] Krajnović, S. and Davidson, L., "Large Eddy Simulation of the Flow Around a Ground Vehicle Body," SAE Paper 01B-64, 2001.

[10] Davidson, L., "LES of Recirculating Flow Without Any Homogeneous Direction: A Dynamic One-Equation Subgrid Model," *2nd Int. Symp. on Turbulence Heat and Mass Transfer*, Delft University Press, Delft, 1997, pp. 481–490.

[11] Emvin, P., *The Full Multigrid Method Applied to Turbulent Flow in Ventilated Enclosures Using Structured and Unstructured Grids*, Ph.D. thesis, Dept. of Thermo and Fluid Dynamics, Chalmers University of Technology, Gothenburg, 1997.

[12] Davidson, L., "Large Eddy Simulation: A Dynamic One-Equation Subgrid Model for Three-Dimensional Recirculating Flow," *11th Int. Symp. on Turbulent Shear Flow*, Vol. 3, Grenoble, 1997, pp. 26.1–26.6.

[13] Krajnović, S. and Davidson, L., "Large-Eddy Simulation of the Flow Around a Surface-Mounted Cube Using a Dynamic One-Equation Subgrid Model," *The First International Symp. on Turbulence and Shear Flow Phenomena*, edited by S. Banerjee and J. Eaton, begell house, inc., New York, Wallingford U.K, 1999, pp. 741–746.

[14] Sohankar, A., Davidson, L., and Norberg, C., "Large Eddy Simulation of Flow Past a Square Cylinder: Comparison of Different Subgrid Scale Models," *ASME: Journal of Fluids Engineering*, Vol. 122, No. 1, 2000, pp. 39–47.

[15] Sohankar, A., Davidson, L., and Norberg, C., "Erratum," *ASME: Journal of Fluids Engineering*, Vol. 122, No. 3, 2000, pp. 643.

[16] Menon, S. and Kim, W.-W., "High Reynolds Number Flow Simulations Using the Localized Dynamic Subgrid-Scale Model," 34th Aerospace Sciences Meeting, AIAA Paper 96-0425, Reno, 1996.

[17] Sohankar, A., *Numerical Investigation of Vortex Shedding Around Square Cylinders at Low Reynolds Number*, Ph.D. thesis, Dept. of Thermo and Fluid Dynamics, Chalmers University of Technology, Gothenburg, 1998.

[18] Krajnović, S., "Large Eddy Simulation of the Flow Around a Three-Dimensional Bluff Body," Thesis for Licentiate of Engineering 00/1, Dept. of Thermo and Fluid Dynamics, Chalmers University of Technology, Gothenburg, Sweden, January 2000.

[19] Reynolds, W., "The Potential and Limitations of Direct and Large Eddy Simulations," *Lecture Notes in Physics*, Vol. 357, 1989.

[20] Krajnović, S., "Large-Eddy Simulation of the Flow Around a Surface-Mounted Single Cube in a Channel," Rept. 98/7, Dept. of Thermo and Fluid Dynamics, Chalmers University of Technology, Gothenburg, 1998.

[21] Jeong, J. and Hussain, F., "On the identification of a vortex," *Journal of Fluid Mechanics*, Vol. 285, 1995, pp. 69–94.